A High Frequency Inductive Power Transfer System for Low-Power Applications in Fresh Water

Xianzao Li
Department of Electrical and Electronic Engineering
Imperial College London
London, UK
xianzao.li21@imperial.ac.uk

Mayue Shi
Department of Electrical and Electronic Engineering
Imperial College London
London, UK
m.shi16@imperial.ac.uk

Paul D. Mitcheson
Department of Electrical and Electronic Engineering
Imperial College London
London, UK
paul.mitcheson@imperial.ac.uk

Eric M. Yeatman
Department of Electrical and Electronic Engineering
Imperial College London
London, UK
e.yeatman@imperial.ac.uk

***Abstract*—This work adopts high-frequency inductive power transfer (HF-IPT) to design an efficient WPT system for low-power sensors and robots in a fresh water environment, and explores the effect of fresh water on coil coupling at different distances. The system configuration is composed of a load-independent Class-EF inverter, PCB coils and a Class-D rectifier with an available gap up to 100 mm. In the experiments, the prototype achieved a peak system efficiency of 66.5% with a power delivery of 8.3 W at a 4.5 cm air gap with a coupling coefficient of 0.1. In a fresh water environment, it still maintained Zero Voltage Switching (ZVS) condition with a gap varying from 4.5 cm to 10 cm, achieving a peak system efficiency of 56.1 % over a wide power range from 0 W to 6.0 W. This study provides design guidelines for employing HF-IPT for low-power energy transfer in fresh water and explores potential factors, including the impact of waterproof enclosures on system performance. The experimental results demonstrate that the load-independent Class-EF inverter can maintain ZVS in fresh water at all distances larger than the designed point (4.5 cm) without any tuning, indicating this topology is a promising candidate for HF-IPT in fresh water.**

Keywords—HF-IPT, load-independent Class-EF, fresh water, IoT

I. Introduction

Underwater wireless sensor networks (UWSNs) are an important layer of the Internet of Things (IoT) for the perception of ambient information in urban pipelines, lakes, oceans, etc. Due to the lifespan and capacity limitations, packaged batteries need to be replaced at regular intervals, which is particularly inconvenient in underwater applications [1]. Also, it is not practical to use wired power delivery as the sensor nodes in an IoT network are usually widely distributed in a large area with low density. Different from the above approaches, WPT doesn't require manual plugging, increasing device mobility and reliability, therefore it is especially preferred in underwater environments.

Underwater WPT can have a variety of transmission mechanisms: capacitive coupled power transfer (CCPT); ultrasonic; laser transmission, IPT, etc [2]. HF-IPT is gaining interest as it balances the relationship between power capacity, efficiency, transmitter size and transmission distance [3]. Current underwater research for IPT mainly focuses on sub-kilowatt power applications in seawater, such as autonomous underwater vehicles (AUVs) due to their importance in industrial applications [4-6]. AUVs can not only perform various underwater tasks as stand-alone underwater probes, such as collecting samples and detecting the environment but also act as energy carriers to charge distributed WSNs by cruising in different clusters. The resonant frequency is usually around hundreds of kilohertz due to high attenuation in seawater (conductivity around 4 *S*/m) [7]. However, in freshwater (conductivity from 0.005 *S*/m to 0.05 *S*/m), eddy current loss has little effect and can be ignored at low frequencies [8], which makes HF-IPT possible.

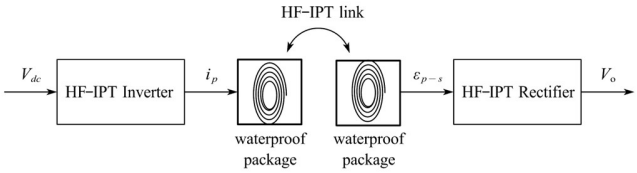


Fig. 1. An underwater HF-IPT system block diagram

To optimize the efficiency in an underwater WPT system, the electric field distribution and eddy current loss in seawater caused by circular coupled coils have been investigated [9,10], and models of circular coil coupling in seawater have also been proposed by modifying the mutual inductance model in the air [11,12]. It is reported that a phase shift phenomenon happens on the primary current and the secondary induced voltage so that it is not 90° anymore, and thus the IPT link is detuned. On this basis, frequency tuning to restrain the eddy current loss, resonant network tuning by introducing a compensation inductance and other methods [11,13] have been widely used to improve the system performance. However, the mechanism of fresh water for megahertz low-power applications is still a gap. Here, we developed an efficient underwater HF-IPT system which is different from previous studies in power level, operating frequency, misalignment resistance, etc.

II. Design of a HF-IPT System For Low-Power Applications in Fresh Water

A basic underwater HF-IPT system structure is illustrated in Fig. 1, in which i_p is the current fed to the primary coil and

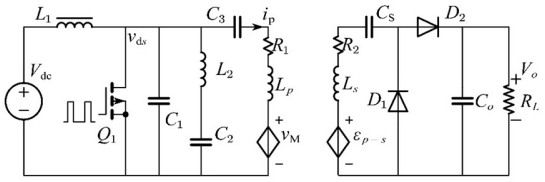


Fig. 2. The circuit topology of the proposed underwater HF-IPT system

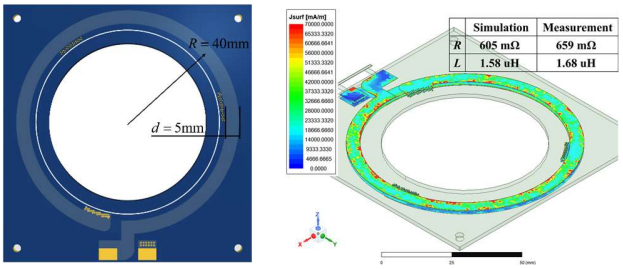


Fig. 3. PCB coil design and simulation. (a) 3d view of the designed PCB coil and (b) the current density distribution on the coil surface with simulation and measured parameters

ε_{p-s} is the secondary induced voltage. For greater integration, inverters/rectifiers can be encapsulated together with coils in waterproof packaging, thereby avoiding the need for extra wired connections between coils and inverters/rectifiers, which leads to reduced parasitic parameters and improved overall system efficiency. The main differences between a typical air application and an underwater application lie in the variance of the transmission medium, such as differences in permittivity and conductivity, potentially causing detuning in the resonant network of IPT. The electrical properties of waterproofing materials are also significant, as certain materials may load on the coils, thereby reducing the overall system performance, such as polyvinyl chloride (PVC). Another potential influence is the air gap between the waterproof packaging and the coil, which may alter the distribution of the electromagnetic field near the coil surface. In addition to the above issues, the inherent mobility of the sensor nodes, influenced by the water, wind and other environmental factors, poses a significant challenge, thus the system must be designed to be insensitive to axial, radial, and even rotational misalignments.

A. Design considerations of the inverters and rectifiers

Taking into account the potential misalignment influenced by the fluidity of freshwater, a load-independent Class-EF inverter stands out as one of the best options [14]. Its feasibility and practicality have been demonstrated in dynamic batteryless drone charging [15] and buried sensor-node charging by drones for agricultural applications [16]. The rectifier adopts a half-wave Class-D rectifier mainly for two purposes. Firstly, current studies indicate that seawater introduces an additional imaginary impedance to the transmit side [11,12]. As the impact of fresh water on the HF-IPT link is still under investigation, a rectifier with a purely resistive input impedance helps quantify the potential influence and thus is preferable, rather than a Class-E rectifier [17] or a Class-EF rectifier [18]. Secondly, given the sensitivity of low-power systems to energy losses, an active rectifier necessitates additional control circuits, thereby increasing system complexity and reducing end-to-end efficiency. The use of an active rectifier is also unnecessary since there is no need for bidirectional power transfer from sensors to AUVs. The proposed circuit topology of the underwater HF-IPT system is shown in Fig. 2. Due to the presence of a certain level of electrical conductivity in fresh water, and considering that eddy current losses are directly proportional to the square of the frequency ($P_{\text{eddy}} \propto f^2$), the operating frequency is set at 6.78 MHz in the current testing stage and not higher.

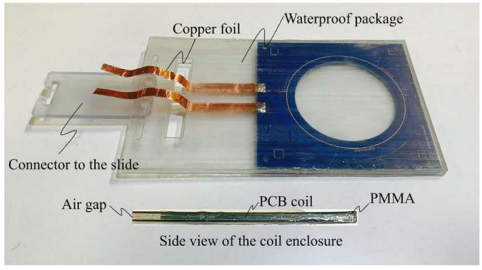


Fig. 4. The photograph of the coil enclosure

B. Design of the PCB coils

Compared to litz wires, PCB coils offer advantages in terms of low cost, stable parameters, and ease of manufacturing. Ideally, only a single PCB layer with a spiral winding should be employed, this approach eliminates proximity effect between turns in one layer and the need for layer transitions within the winding [19]. Simultaneously, it's crucial for the coil inductance to meet a specific value to ensure that the current output from a Class-EF inverter is sinusoidal. Therefore, utilizing multiple helical PCB layers is the best option.

The designed primary and secondary PCB coils are identical and have a diameter of 8 cm and a trace width of 5 mm. It is a 4-layer single-turn design with 1 oz copper thickness. The coil design was simulated using Ansys HFSS module, and the PCB coil was measured with a Keysight E5061B network analyzer. The coil diagram, simulation and measurement results at 6.78 MHz are shown in Fig. 3. Fig. 3(a) shows a 3D view of the designed PCB coil in Altium Designer. In Fig. 3 (b), the current density primarily concentrates at the edge of each turn due to the skin effect and proximity effect between layers. Unlike PCB planar transformers, this issue is challenging to address as it is not possible to carry antiparallel currents in PCB air-core inductors. One improvement to mitigate the mentioned effect is adopting a litz wire structure for PCBs [20].

C. Design of the transmit/receive sides

The PCB coils are packaged in a flat 3D printed box made of *VeroClear* (Creatz3D) material for waterproofing. The two acrylic panels, each with a thickness of 1 mm, encase the PCB coil at the center, creating a 1 mm air gap between the coil surface and the inner wall of the package box, as illustrated in Fig. 4. The connection between the coil and the inverter/rectifier is established through a 6 mm-wide, 10 cm-long copper foil. Compared to using multi-stranded AWG wires, copper foil not only possesses sufficient current-carrying capacity, but its flat

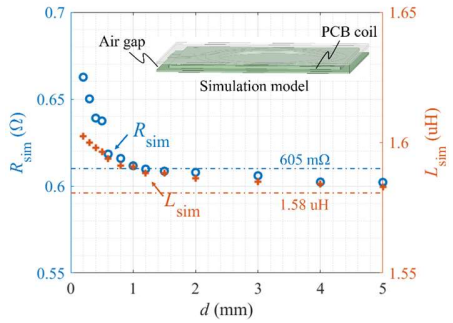


Fig. 5. The relationship of coils parameters and the width of air gap between the coil surface and the inner wall of the waterproof package.

structure is also advantageous for insertion into the waterproof enclosure to connect with the coil interface. Additionally, the distribution parameters of copper foil are smaller than those of AWG wires, preventing the connection section from becoming an additional *LC* high-order resonant network.

When passing through different medium surfaces, the distribution of the electromagnetic field may undergo changes. Therefore, variations in the air gap width could impact the HF-IPT link, primarily manifested in changes to coil self-inductance and mutual inductance. Simulation results from Ansys HFSS indicate that the AC resistance and inductance of the coil in fresh water only slightly decrease with an increase in air gap width, and when the air gap width reaches a certain level (approximately 1 mm in this design), the impact of the waterproof enclosure tends to stabilize. The dot-dash line shows the simulation value of coil impedance without any waterproof enclosure, as shown in Fig. 5. In addition, the magnetic field distribution in the vicinity of the coil has little difference.

In summary, compared to the coil impedance in air, the width of the air gap or the presence of waterproof material still has some impact on the PCB coil self-inductance and may retune the resonant network. However, the influence is not significant when the air gap is wide enough, ranging from 2 to 5 mm, as depicted in Fig. 5.

D. Optimal parameters design of the system

A T-WPT model based on a Class-EF inverter is shown in Fig. 6. For any resonant compensation network and rectifiers, a general optimal parameters design method is derived as follows. The optimal AC impedance of the secondary side is

$$Z_{ac,opt} = R_2\sqrt{1+k^2Q_1Q_2} - j\omega L_s \tag{1}$$

Where R_2 is the equivalent series resistance (ESR) of the secondary coil, Q_1 and Q_2 are the quality factors of the coil. For single capacitance with series compensation, the AC impedance of the secondary side can also be written as

$$Z_{ac} = Z_{\text{in,rect}}(R_L) + \frac{1}{j\omega C_s} \tag{2}$$

Or for single capacitance with parallel compensation,

$$Z_{ac} = \frac{Z_{\text{in,rect}}(R_L)}{1 + j\omega C_s Z_{\text{in,rect}}(R_L)} \tag{3}$$

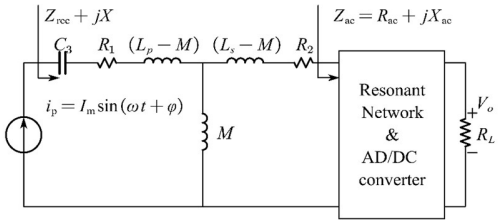


Fig. 6. Impedance analysis of a general T-WPT model with Class-EF inverter and arbitrary receiver.

The $Z_{\text{in,rect}}(R_L)$ is the input impedance of the chosen rectifier, which is usually a function of the load resistance R_L. The reflected impedance of the receiver to the transmitter side is

$$Z_{\text{rec}} + jX = \frac{\omega M[\omega M - (\omega L_s + X_{ac}) + j(R_2 + R_{ac})]}{(R_2 + R_{ac}) + j(\omega L_s + X_{ac})} + R_1 + \left(j\omega L_p + \frac{1}{j\omega C_3}\right) - j\omega M \tag{4}$$

Where $Z_{ac} = R_{ac} + jX_{ac}$ and $jX = j\omega L_s + \frac{1}{j\omega C_3}$. Apparently, when $X_{ac} = -\omega L_s$, Z_{rec} is resistive and the reflected load resistance for load-independent Class-EF inverter is

$$Z_{\text{rec}} = R_1 + \frac{(\omega M)^2}{R_2 + R_{ac,opt}} \tag{5}$$

Based on the above design procedure and given the coil parameters in the previous Section II Part B, the target output power $P_o = 10$ W and the coupling coefficient $k = 0.1$ (corresponding to a distance of 4.5 cm by FEA simulation), all parameters of the system can be calculated. For SS compensation and half-wave Class-D rectifier, the optimal load resistance is

$$R_{L,opt} = \frac{\pi^2}{2} R_{ac,opt} \tag{6}$$

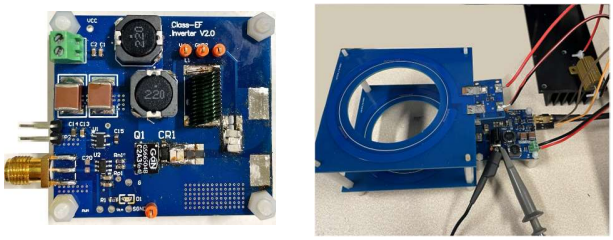
According to (5), the amplitude of the inverter output current is $I_{\text{m}} = \sqrt{2P_o/Z_{\text{rec}}}$. Applying the load-independent Class-EF inverter design criterion from Table II in [14], in the special case of maximum power-output capability c_p, duty cycle $D = 0.3$, eigenfrequency coefficient $q_1 = 1/\omega\sqrt{L_2C_2} = 1.66$ and $C_1/C_2 = 1.2706$. By selecting the load factor $p = 2$ (denoted in [12]), the design equations are as follows.

$$\begin{gathered} \omega R_L C_1 = 0.1772 \\ \omega X C_1 = 0.3402 \\ \frac{I_m R_L}{V_{in}} = 0.4409 \\ P_o \frac{R_L}{V_{in}^2} = 0.0972 \\ c_p = 0.0882 \end{gathered} \tag{7}$$

Where R_L is the maximum load of the inverter and X is the residual reactance of C_3 and L_p. R_L refers to Z_{rec} in (5) for a WPT system design. The implementation of the system is shown in Table I. Pictures of the Class-EF inverter and initial testing platform in air are given in Fig. 7.

TABLE I. IMPLEMENTATION OF SYSTEM

Component	Value	Description
L_1	2×22 uH	WE-PD 22uH 3A
C_1	400 pF	KEMET C0G
C_2	524 pF	KEMET C0G
C_3	398 pF	KEMET C0G
L_2	390 nH	Coilcraft 2929SQ-391GEC
R_1 & R_2	0.659 Ω	ESR of PCB coil
L_p & L_s	1.68 uH	Inductance of PCB coil
C_s	320 pF	KEMET C0G
$R_{L,opt}$	30 Ω	Load resistance
D_1 & D_2	Diodes BAT165-HG3/H	
Q_1	GaNfet GS66504B 650V, 15A	
Gate Drive	LM5114	



(a) (b)

Fig. 7. Photograph of system circuits. (a) Designed load-independent Class-EF inverter and (b) Platform in air for initial testing.

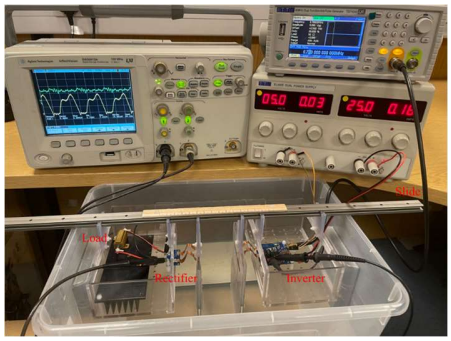


Fig. 8. The experimental setup

III. EXPERIMENTAL RESULTS

To explore the impact of freshwater on the HF-IPT link, an experimental setup is built, as shown in Fig. 8. To minimize the length of the required copper foil connection, the inverter and rectifier hang below the slide in a box. As the copper foil used for connection introduces an additional inductance to the inverter and rectifier, the coil's resistance and inductance with the copper foil were 748 mΩ and 1.80 uH. Consequently, the resonant capacitance should be readjusted to C_3 = 362.4 pF and C_s = 306.1 pF and actual retuned value of capacitance is C_3 = 363.4 pF and C_s =304.7 pF. A slide is employed to alter the distance, simulating axial misalignment, while radial misalignment can be mimicked by adjusting the distance between the centre of the slide and the waterproof enclosure, in which axial distance ranges from 0 to 10 cm, while radial misalignment ranges from 0 to 4 cm, as depicted in Fig. 9. Due to the fundamental nature of both axial misalignment and radial misalignment as changes in the coupling coefficient k, the current experiments have only conducted tests on axial misalignment.

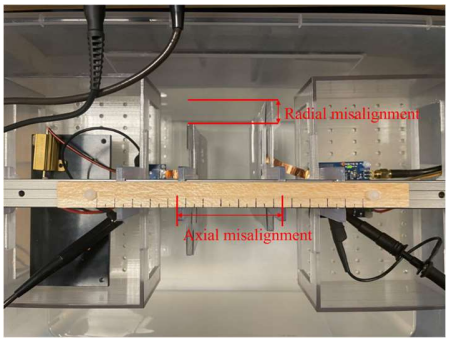


Fig. 9. Axial and radial misalignment for the system

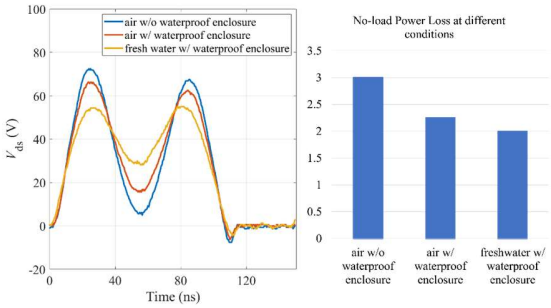


Fig. 10. No load test of the Class-EF inverter. (a) drain waveforms and (b) no load loss at different conditions.

A. No load test of the system

The designed load-independent Class-EF inverter is initially tested in air and fresh water to check out the performance and influence of waterproof enclosure. Without waterproof enclosure, the no-load loss of the inverter and primary coil is 3 W, mainly comes from the AC resistance losses in the coil, which amount to approximately 1.1 W, and the ESR losses of resonant capacitor C_3. Previous experiments demonstrate that using a smaller package for C_3 contributes to an increase in system efficiency. For instance, changing the package of C_3 from 1206 to 0603 results in an approximate 10% improvement in system efficiency. With the waterproof enclosure, the no-load loss of the inverter and primary coil in air is 2.25 W, and in fresh water, it is 2 W. The changes in the shape of drain waveforms and no-load losses suggest that both the waterproof enclosure and the presence of freshwater slightly retune the inverter.

B. Test of the system in air

The measured coupling coefficient k ranges from 0.1% to 10%. The maximum value of the coupling coefficient occurs when the two coils are perfectly aligned and separated by 4.5 cm,

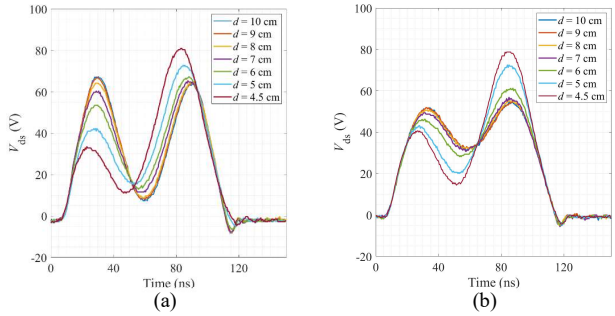


Fig. 11. The drain waveforms. (a) v_{ds} in air and (b) v_{ds} in fresh water.

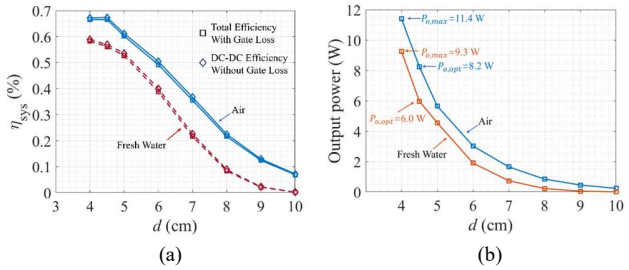


Fig. 12. The system performance in air and fresh water. (a) system efficiency and (b) output power.

while the minimum value occurs when the two coils have a radial misalignment of 4 cm and are separated by 10 cm.

The drain waveforms of the system from 4.5 cm to 10 cm with only an axial distance change, as shown in Fig. 11(a), and the ZVS condition is achieved at any distance larger than 4.5 cm (the design point) as a load-independent Class-EF inverter keeps its characteristics from zero to finite load resistances. Fig. 12(a) gives the system efficiency with and without gate loss and Fig. 12(b) shows the output power with only axial separation. The maximum output power, achieved at d = 4 cm, is 11.4 W, while the output power at d = 4.5 cm (the designed point) is 8.2 W. The maximum system efficiency is 66.5%, considering the gate loss, and 67.3% without gate loss. Both efficiency values are attained at d = 4.5 cm. Comparing the system performance with and without a waterproof enclosure (Fig. 7), the system's efficiency and output power did not degrade due to the waterproofing, and ZVS condition was maintained. This validates the previous conclusion that the chosen waterproofing method has minimal impact on the HF-IPT link.

C. *Test of the system in fresh water*

The system is further tested in fresh water. The inverter still keeps ZVS condition without any additional tuning. The drain waveforms at different transmission distances are given in Fig. 11(b). The end-to-end efficiency and output power are given in Fig. 12. The maximum output power in fresh water is 9.3 W achieved at d = 4 cm, while the output power at d = 4.5 cm (the designed point) is 6.0 W. The maximum system efficiency considering the gate loss is 58.2%, achieved at d = 4 cm. However, when d < 4.5 cm, the reflected impedance is larger than the designed value, causing ZVS lost. Therefore, the optimal operation point for the system is at d = 4.5 cm, with

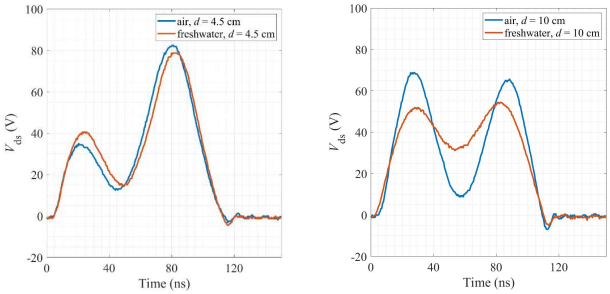


Fig. 13. Comparison of the drain waveforms. (a) v_{ds} in air and (b) v_{ds} in fresh water.

$P_{\mathrm{o|max}}$ = 6.0 W and $\eta_{\mathrm{sys|max}}$ = 56.1%. Although the highest system efficiency and output power both drops in fresh water, a big advantage is that no additional tuning is needed to make the system work in fresh water when it is perfectly tuned in air. It still can be noticed that the drain waveform changes when the medium changes, which will be discussed in detail in the next part.

D. *Comparison and analysis*

Fig. 13 gives a close view of how the drain waveforms vary in different mediums. As the two coils gradually move apart, the shape difference of the drain waveform also gradually increases. Achieving ZVS conditions in different mediums simultaneously is attributed to the system's practical tolerance for ZVS conditions when the load exhibits slight inductive or capacitive impedance. This can be determined by manually setting certain ZVS boundaries, such as drain voltage, current, temperature, etc. As the unique reflected impedance introduces a unique v_{M} in the inverter side, the shape of drain waveforms can be determined by solving high-order differential equations in a Class-EF circuit. Thus, there is a relationship between the reflected load impedance and the drain waveforms, allowing the drain waveform to be used for characterizing the imaginary part introduced by freshwater.

IV. Conclusion and Future Work

This work, for the first time, investigated an underwater HF-IPT system utilizing a load-independent Class-EF inverter, with significant advantages including a wide-range ZVS, no additional tuning required in fresh water, and acceptable efficiency and output power reduction in fresh water. The findings reveal that the presence of freshwater does not break the ZVS condition boundary of the system, highlighting the load-independent Class-EF HF-IPT system as a promising choice for energizing sensor nodes and low-power robots in freshwater environments. Initial experiments also indicate that the impact of eddy current losses on the system at 6.78 MHz is acceptable, resulting in only a 10% efficiency drop. Therefore, selecting a higher operating frequency becomes a viable option to enhance power density. In addition, there exists a trade-off for the optimal resonant frequency in fresh water. Increasing the frequency leads to a rise in eddy current loss but also an improvement in the efficiency of the HF-IPT link.

Future work involves modelling the HF-IPT link in freshwater using information from the drain waveforms, eliminating the copper foil for connection and integrating the system, and optimizing the coil design to minimize losses. Finally, after integrating a DC/DC module to stabilize the output voltage, the system will be utilized for charging practical underwater sensors.

ACKNOWLEDGMENT

The authors would like to acknowledge Imperial College London for the funding sources.

REFERENCES

[1] Y. Guo, X. Liu, and C. Chen, “Research on hybrid cooperative charging scheduling schemes in underwater sensor networks,” *IEEE Access*, vol. 7, pp. 156 452–156 462, 2019.

[2] S. D. Barman, A. W. Reza, N. Kumar, M. E. Karim, and A. B. Munir, “Wireless powering by magnetic resonant coupling: Recent trends in wireless power transfer system and its applications,” *Renewable and Sustainable Energy Reviews*, vol. 51, pp. 1525–1552, 2015.

[3] S. Y. R. Hui, W. Zhong and C. K. Lee, "A Critical Review of Recent Progress in Mid-Range Wireless Power Transfer," in *IEEE Transactions on Power Electronics*, vol. 29, no. 9, pp. 4500-4511, Sept. 2014.

[4] Z. Yan, B. Song, Y. Zhang, K. Zhang, Z. Mao, and Y. Hu, “A rotation-free wireless power transfer system with stable output power and efficiency for autonomous underwater vehicles,” *IEEE Transactions on Power Electronics*, vol. 34, no. 5, pp. 4005–4008, 2019.

[5] D. Wang, S. Cui, J. Zhang, Z. Bie, K. Song, and C. Zhu, “A novel arc-shaped lightweight magnetic coupler for auv wireless power transfer,” *IEEE Transactions on Industry Applications*, vol. 58, no. 1, pp. 1315–1329, 2022.

[6] Y. Zeng, C. Rong, C. Lu, X. Tao, X. Liu, R. Liu, and M. Liu, “Misalignment in-sensitive wireless power transfer system using a hybrid transmitter for autonomous underwater vehicles,” *IEEE Transactions on Industry Applications*, vol. 58, no. 1, pp. 1298–1306, 2022.

[7] Z. Yan, Y. Zhang, T. Kan, F. Lu, K. Zhang, B. Song, and C. Mi, “Eddy current loss analysis of underwater wireless power transfer system,” in *2018 IEEE Transportation Electrification Conference and Expo (ITEC)*, 2018, pp. 881–884.

[8] Z. Liu, L. Wang, Y. Guo, and C. Tao, “Eddy current loss analysis of wireless power transfer system for autonomous underwater vehicles,” in *2020 IEEE PELS Workshop on Emerging Technologies: Wireless Power Transfer (WoW)*, 2020, pp. 283–287.

[9] J. Kim et al., "Analysis of Eddy Current Loss for Wireless Power Transfer in Conductive Medium Using Z-parameters Method," *2020 IEEE Wireless Power Transfer Conference (WPTC)*, 2020, pp. 432-434.

[10] Jie Zhou, De-jun Li, Ying Chen, "Frequency selection of an inductive contactless power transmission system for ocean observing, " in *Ocean Engineering*, vol. 60, 2013, Pages 175-185.

[11] K. Zhang, Y. Ma, Z. Yan, Z. Di, B. Song and A. P. Hu, "Eddy Current Loss and Detuning Effect of Seawater on Wireless Power Transfer," in *IEEE Journal of Emerging and Selected Topics in Power Electronics,* vol. 8, no. 1, pp. 909-917, March 2020.

[12] W. Li, J. Zhu, Y. Wang and B. Liu, "Modeling and Characteristic Analysis of Magnetic Coupling Mechanism in Seawater Environment," in *IEEE Transactions on Magnetics*, vol. 58, no. 9, pp. 1-6, Sept. 2022.

[13] Z. Yan et al., "Frequency Optimization of a Loosely Coupled Underwater Wireless Power Transfer System Considering Eddy Current Loss," in *IEEE Transactions on Industrial Electronics*, vol. 66, no. 5, pp. 3468-3476, May 2019.

[14] S. Aldhaher, D. C. Yates and P. D. Mitcheson, "Load-Independent Class E/EF Inverters and Rectifiers for MHz-Switching Applications," in *IEEE Transactions on Power Electronics*, vol. 33, no. 10, pp. 8270-8287, Oct. 2018.

[15] J. M. Arteaga, S. Aldhaher, G. Kkelis, C. Kwan, D. C. Yates and P. D. Mitcheson, "Dynamic Capabilities of Multi-MHz Inductive Power Transfer Systems Demonstrated With Batteryless Drones," in *IEEE Transactions on Power Electronics*, vol. 34, no. 6, pp. 5093-5104, June 2019.

[16] J. M. Arteaga et al., "High-Frequency Inductive Power Transfer Through Soil for Agricultural Applications," in *IEEE Transactions on Power Electronics*, vol. 38, no. 11, pp. 13415-13429, Nov. 2023.

[17] G. Kkelis, D. C. Yates and P. D. Mitcheson, "Class-E Half-Wave Zero dv/dt Rectifiers for Inductive Power Transfer," in *IEEE Transactions on Power Electronics*, vol. 32, no. 11, pp. 8322-8337, Nov. 2017.

[18] S. Aldhaher, D. C. Yates and P. D. Mitcheson, "Design and Development of a Class EF_2 Inverter and Rectifier for Multimegahertz Wireless Power Transfer Systems," in *IEEE Transactions on Power Electronics*, vol. 31, no. 12, pp. 8138-8150, Dec. 2016.

[19] J. Schäfer, D. Bortis and J. W. Kolar, "Novel Highly Efficient/Compact Automotive PCB Winding Inductors Based on the Compensating Air-Gap Fringing Field Concept," in *IEEE Transactions on Power Electronics*, vol. 35, no. 9, pp. 9617-9631, Sept. 2020.

[20] I. Lope, C. Carretero, J. Acero, R. Alonso and J. M. Burdio, "Frequency-Dependent Resistance of Planar Coils in Printed Circuit Board With Litz Structure," in *IEEE Transactions on Magnetics*, vol. 50, no. 12, pp. 1-9, Dec. 2014.